

Article

Identification of Pine Wilt Disease-Infested Stands Based on Single- and Multi-Temporal Medium-Resolution Satellite Data

Jinjie Kuang ¹, Linfeng Yu ^{1,2}, Quan Zhou ¹, Dewei Wu ^{1,3}, Lili Ren ¹ and Youqing Luo ^{1,*}

¹ Key Laboratory for Forest Pest Control, College for Forestry, Beijing Forestry University, Beijing 100083, China; jinjiakuang2023@163.com (J.K.)

² Institute of Forest Resource Information Techniques, Beijing 100091, China

³ Liaoning Provincial Station of Forest Pest Control and Quarantin, Shenyang 110804, China

* Correspondence: yqluo@bjfu.edu.cn; Tel.: +86-6233-6840

Abstract: Pine wilt disease (PWD) is known for its high lethality and rapid transmission, earning it the name “cancer of the pine tree”. The prompt removal of infested pine trees is an effective measure for preventing and controlling pine wilt disease. Accurate and efficient monitoring technologies are crucial for the scientific prevention and control of this plant disease. Currently, numerous remote sensing monitoring studies have been conducted on pine wilt disease. However, there is limited research on the temporal identification of PWD-infested forest stands over large areas. To build classification models, this study utilized three machine learning algorithms: artificial neural network (ANN), random forest (RF), and support vector machine (SVM). We aimed to investigate the effectiveness of single-temporal and multi-temporal Landsat and Sentinel-2 satellite images PWD-infested forest stands detection. The results indicated that, at a spatial resolution of 30 m, Landsat-9 and Sentinel-2 remote sensing images effectively identified PWD-infested forest stands, with classification accuracies of 77.87% and 78.91%, respectively. Higher spatial resolutions in Sentinel-2 remote sensing images were associated with improved identification capabilities. Furthermore, multi-temporal Landsat satellite data (with a classification accuracy of 85.95%) significantly enhanced the performance of the monitoring model compared to single-temporal Landsat satellite data (with a classification accuracy of 77.87%). The RGI difference was found to be the optimal vegetation index. In conclusion, by combining multi-temporal and single-time-phase Landsat remote sensing data, a monitoring model for PWD-infested forest stands was constructed. It achieved a classification accuracy of 88.26%. In this study, a higher accuracy in identifying pine wilt disease and a lower economic cost were achieved by Landsat and Sentinel images, offering valuable insights for the management of pine wilt disease.

Keywords: Landsat; Sentinel-2; single-temporal; multi-temporal; RGI difference



Citation: Kuang, J.; Yu, L.; Zhou, Q.; Wu, D.; Ren, L.; Luo, Y. Identification of Pine Wilt Disease-Infested Stands Based on Single- and Multi-Temporal Medium-Resolution Satellite Data.

Forests **2024**, *15*, 596. <https://doi.org/10.3390/f15040596>

Academic Editor: Young-Seuk Park

Received: 5 February 2024

Revised: 4 March 2024

Accepted: 19 March 2024

Published: 25 March 2024



Copyright: © 2024 by the authors. Licensee MDPI, Basel, Switzerland. This article is an open access article distributed under the terms and conditions of the Creative Commons Attribution (CC BY) license (<https://creativecommons.org/licenses/by/4.0/>).

1. Introduction

Pine wilt disease is a destructive pine disease caused by the pinewood nematode (*Bursaphelenchus xylophilus*). PWD is characterized by multiple transmission pathways, rapid host mortality, and challenging management [1]. It takes only about 40 days from the appearance of symptoms for an infested pine to die, and if the infested pine is not cleared promptly, an entire pine forest can be destroyed within 2–3 years [2]. North America is considered the origin of pine wilt disease [3]. Since its discovery in 1982 at the Zhongshan Mausoleum in Nanjing, China, the disease has spread to 19 provinces and 731 county-level administrative districts, and due to the increasing adaptability of pine wilt disease, it has gradually invaded the middle and high latitudes of China. More than 1.4 million trees in China have succumbed to pine wilt disease, causing significant ecological damage. Due to it causing significant ecological damage [4,5], the prevention and control of the disease are critical.

The timely detection and removal of pine wilt disease-infested wood are essential for controlling pine wilt disease. Initially, the monitoring of pine wilt disease relied on manual ground surveys. However, this approach was constrained by climate, terrain, and other conditions, resulting in poor real-time performance, high costs, low efficiency, and the inability to conduct macro-dynamic monitoring. This limitation has hindered the guidance of pine wilt disease prevention and control efforts. The development of remote sensing technology opens up new possibilities for monitoring pine wilt disease, with optical remote sensing being the most widely used method. The spectral response of plants to pests and diseases reflects changes in pigmentation, water content, morphology, and structure caused by these factors. This response is multifunctional and closely related to the characteristics of a specific pest or disease [6]. During pinewood nematode infestation, photosynthetic physiological parameters within the infested wood are altered, resulting in significant external symptoms in trees. Needles lose water and change color, transitioning from green to yellow or red, but they do not fall off, ultimately leading to the death of the entire plant. Changes in the canopy of infested trees induce abnormalities in plant reflectance, altering spectral characteristics and causing variations in spectral values and texture structure in remotely sensed images. This makes remote sensing monitoring of infested trees feasible [7–9].

Currently, UAV remote sensing is widely employed for monitoring pine wilt nematode disease due to its simplicity and timeliness [10]. Wu et al. determined the optimal monitoring time frames for each infection stage of pine wilt disease using multi-temporal unmanned aerial vehicle multispectral data [11]. Lee used a DJI M600 Pro equipped with a HeadWall nano hyperspectral sensor to successfully identify pine wilt disease-infested wood [12]. Another study found that the use of UVA hyperspectral and multispectral data enables the identification of pine trees infested by pinewood nematode before symptoms appear [13]. However, hyperspectral data are costly, challenging to process, and present difficulties in monitoring pine wilt disease over large areas due to limitations imposed by drone range, weather conditions, and other factors.

Satellite remote sensing, on the other hand, offers broad spatial coverage, abundant data, and lower cost [14], making it suitable for large-area monitoring. Previous researchers employed high-resolution satellites for the single-tree-scale monitoring of infested pine; for example, Zhang et al. achieved the extraction of single infested pine trees in complex forest stands using PlanetScope satellites [15]; Qu et al. identified discolored pines in remote sensing images using deep learning and Jilin-1 satellites [16]; additionally, Jiao et al. evaluated Terrestrial Ecosystem Carbon Inventory Satellite's ability to recognize color-changing standing trees [17]. However, high-resolution satellites are generally expensive, and obtaining multi-temporal data is challenging. In comparison, medium-resolution satellites like Landsat and Sentinel-2 have swath widths of 185 km and 290 km, with revisit periods of 16 days and 10 days, respectively. They can be obtained free of charge and have NIR and SWIR bands that effectively monitor vegetation health [18]. Therefore, they exhibit the characteristics of wide coverage, low cost, and rich historical data, making them highly promising for forest management [19]. Lin monitored oak tree pest infestation based on Landsat-8 satellite data and the random forest algorithm [20]; Abdullah et al. found that Sentinel-2 satellite data were more sensitive to changes in trees caused by the green attack stage of the bark beetle compared to Landsat-8 satellite data [21]. These studies demonstrated the effectiveness of medium-resolution satellite imagery in identifying pests and diseases affecting forest stands.

Currently, there are limited studies on pine wilt disease monitoring using Landsat and Sentinel-2 satellite data. Qiu and Zong investigated various combinations of machine learning algorithms and vegetation indices to identify stands infested with pinewood nematodes using Landsat-8 and Sentinel-2 single-temporal satellite remote sensing data. The accuracy of the optimal monitoring model was 79.3% [18]. However, further research is required to assess the capability of multi-temporal medium-resolution satellite data in discriminating pine wilt disease-infested stands. Therefore, the main objectives of this experiment

were as follows: (1) to compare the capability of Landsat-9 and Sentinel-2 satellite data in identifying pine wilt disease-infested stands at the same spatial resolution (30 m); (2) to resample Sentinel-2 satellite data to different spatial resolutions (10 m vs. 30 m) to assess their efficacy in discriminating pine wilt-infested stands; and (3) to explore the potential of multi-temporal Landsat satellite data in identifying pine wilt disease-infested stands.

2. Materials and Methods

2.1. Overview of the Study Area

The study site is situated in Muping District, Yantai City, Shandong Province, China (N 37°27'8.9172", E 121°42'2.916"). The region experiences a warm-temperate East Asian monsoon continental climate, with an average annual temperature of 11.6 °C and a precipitation of 737.2 mm. Pine wilt disease was first detected in Muping District in 2014, and it began to exhibit accelerated proliferation and spread around 2018. By 2019, the infested area had exceeded 13,900 hm², indicating a high need for management [22]. Currently, the area is experiencing significant damage, making it suitable as an experimental sample site. Following comprehensive on-site surveys, we selected five pine forests infested with pine wilt disease as experimental sites (Figure 1). These sites within the study area are severely infested by pine wilt disease, which is the primary factor causing harm to the pine forests in this region. Furthermore, the study area features a relatively flat terrain, encompassing a total area of around 80 ha. The dominant species is Japanese black pine (*Pinus thunbergii* Parl.), with a small amount of Japanese red pine (*Pinus densiflora* Siebold & Zucc).

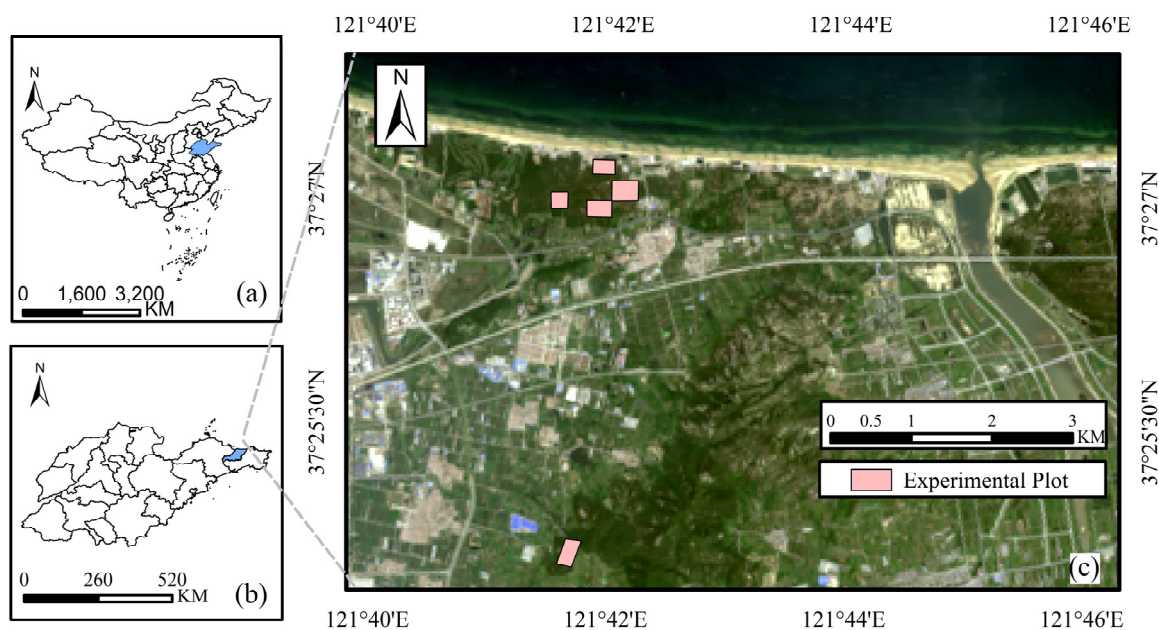


Figure 1. (a) Shandong Province in China. (b) Muping District in Shandong Province. (c) Location of study area.

2.2. Data Acquisition

2.2.1. Remote Sensing Data from UAV

During July–October 2022, DJI Inspire 2 and Mavic 2 Pro (DJI, Shenzhen, China) were employed to capture UAV visible light images with a ground resolution of approximately 1.3–1.6 cm. The bypass overlap rate was set to 85%, the heading overlap rate to 80%, and the flight speed to 5 m/s. Considering the study area's altitude, the flight altitude ranged from 50 to 65 m. Simultaneously, considering the availability of satellite images in which no clouds obscured the plots, we selected two UAV images, dated 13 September 2022 and 1 October 2022 (Figure 2), to extract healthy and infested sample squares as reference data for satellite remote sensing. Moreover, during this period, the main deciduous trees had

not yet undergone significant color changes, facilitating the identification and statistical analysis of infested trees [16].

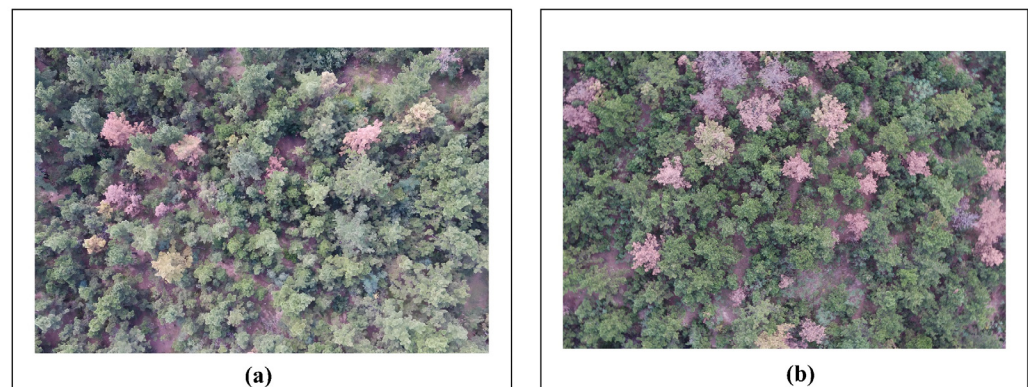


Figure 2. (a) Partial image of UVA remote sensing data captured on 13 September 2022. (b) Partial image of UVA remote sensing data captured on 1 October 2022.

2.2.2. Satellite Remote Sensing Data

The satellite data utilized in this study were obtained from Landsat series satellites (including Landsat 5 (TM5), 7 (ETM+), 8 (OLI), and 9 (OLI-2)) with a spatial resolution of 30 m and Sentinel-2 (MSI) satellites with spatial resolutions of 10 and 30 m. The data sources and bands of the satellites used in this experiment are detailed in Table 1. Due to space limitations, only band and sensor information for Landsat-9 and Sentinel-2A is presented.

Table 1. Spectral regions of Landsat OLI and Sentinel-2A MSI sensors.

Band	OLI-2 (Landsat-9)		MSI (Sentinel-2A)		
	Spectral Regions (μm)	Band	Central Wavelength (μm)	Bandwidth (μm)	
Coastal	0.43–0.45	Coastal	0.443		0.027
Blue	0.45–0.51	Blue	0.49		0.098
Green	0.53–0.59	Green	0.56		0.045
Red	0.64–0.67	Red	0.665		0.038
NIR	0.85–0.88	Red Edge 1	0.705		0.019
SWIR 1	1.57–1.65	Red Edge 2	0.740		0.018
SWIR 2	2.11–2.29	Red Edge 3	0.783		0.028
		NIR	0.842		0.145
		Narrow NIR	0.865		0.033
		Water vapor	0.945		0.026
		SWIR 1	1.61		0.143
		SWIR 2	2.19		0.242

Landsat series L1-level data for the years 2008–2013 and 2022 were obtained from the USGS (<http://www.usgs.gov/>), excluding 2011 Landsat data due to excessive cloud cover. We used total of 12 scenes of satellite data (Table 2), primarily captured in September and October, aligning with the months of drone imagery.

Sentinel-2 satellite L1-level data were obtained from the Copernicus Data Space Ecosystem website (<http://dataspace.copernicus.eu/>). None of the selected satellite remote sensing images for this study exhibited cloud cover in the study area.

Table 2. Data sources and dates.

Date	Data Source	Number of Bands
15 September 2008	Landsat-7	6
1 October 2008		
2 September 2009	Landsat-7	6
4 October 2009		
13 September 2010	Landsat-5	6
15 October 2010		
1 September 2012	Landsat-7	6
28 October 2012		
2 August 2013	Landsat-8	7
23 October 2013		
6 September 2022	Landsat-9	7
8 October 2022		
1 September 2022	Sentinel-2	12
5 October 2022		

2.3. Data Processing

2.3.1. Satellite Data Processing

The pre-processing steps for Landsat series satellites consist of three main procedures: (1) image cropping; (2) radiometric calibration; (3) atmospheric correction. Landsat images were pre-processed in ENVI 5.6 (Exelis Visual Information Solutions, Inc., United States), which enhanced the reliability and accuracy of the Landsat satellite images. The study area was extracted from Landsat images by vector data in ENVI 5.6. Radiometric calibration was conducted through the radiometric Calibration tool in ENVI, with calibration parameters according to FLAASH Settings. Atmospheric corrections were carried out using the FLAASH Atmospheric Correction tool in ENVI.

Sentinel-2 satellite data underwent radiometric calibration and atmospheric correction using the Sen2Cor plug-in in SNAP 9.0.0 software (European Space Agency, Paris, France). Subsequently, the pre-processed data were resampled to achieve a final spatial resolution of 10 m and 30 m for Sentinel-2 data.

2.3.2. UVA Data Processing

To maintain spatial and temporal consistency between UAV and satellite images, we manually selected control points for geo-alignment using the Georeferencing tool in ArcGIS 10.4 (Esri, Redlands, CA, USA). These ground control points were chosen based on prominent landmarks in UAV and satellite images, such as obvious water bodies, houses, and road turning points. After geographically aligning the UAV data with the satellite data, 30 m × 30 m and 10 m × 10 m sample squares were delineated in the UAV images based on the location and size of the satellite pixels. The spatial resolution matched that of the satellite remote sensing data. We visually interpreted and distinguished healthy and infested trees using the presence or absence of discolored pine in the sample plots as criteria; a plot was considered healthy if there were no variegated pines and infested if variegated pines were present. Simultaneously, in the sample plots, we confirmed that discolored pine trees resulted from pinewood nematode infestation using the Bellman funnel method, morphology characters, and molecular barcodes. Identification in UAV images yielded 74 healthy pixels and 80 infested pixels in the 30 m resolution satellite images. In the 10 m resolution satellite image, there were 590 healthy pixels and 276 infested pixels.

2.4. Modeling of Pine Wilt Disease Surveillance

2.4.1. Model for Monitoring Pine Wilt Disease with Single-Temporal Satellite Remote Sensing Data

Spectral reflectance and vegetation indices (VIs) can partially reflect the health of vegetation [23]. Building on previous research [15,18], we chose 10 vegetation indices (Table 3) along with the spectral reflectance of Landsat-9 and Sentinel-2 bands (including

10 m and 30 m resolutions) as model characteristic parameters. Artificial neural network, random forest, and support vector machine algorithms were employed to construct the model. The random forest importance ranking method was utilized to identify and filter sensitive feature parameters. We compared the model accuracy of the Sentinel-2 dataset at 10 m and 30 m resolutions using different machine learning algorithms to elucidate the impact of spatial resolutions on the accuracy of the Sentinel-2 model.

Table 3. Vegetation index names and formula.

Name	Formula	Ref.
Chlorophyll Vegetation Index (CVI)	$(\text{NIR} * \text{RED}) / (\text{GREEN} * \text{GREEN})$	[24]
Green Leaf Index (GLI)	$(2 * \text{GREEN} - \text{RED} - \text{BLUE}) / (2 * \text{GREEN} + \text{RED} + \text{BLUE})$	[25]
Blue-wide Dynamic Range Vegetation Index (BWD RVI)	$(0.1 * \text{NIR} - \text{BLUE}) / (0.1 * \text{NIR} + \text{BLUE})$	[26]
Normalized Difference Green/Red (NGRDI)	$(\text{GREEN} - \text{RED}) / (\text{GREEN} + \text{RED})$	[27]
Atmospherically Resistant Vegetation Index 2 (ARVI2)	$-0.18 + 1.17 * ((\text{NIR} - \text{RED}) / (\text{NIR} + \text{RED}))$	[28]
Chlorophyll Index Green (CIgreen)	$(\text{NIR} / \text{GREEN}) - 1$	[27]
Enhanced Vegetation Index 2 (EVI2)	$2.4 * (\text{NIR} - \text{RED}) / (\text{NIR} + \text{RED} + 1)$	[29]
Specific Leaf Area Vegetation Index (SLAVI)	$\text{NIR} / (\text{RED} + \text{SWIR})$	[30]
Normalized Difference Rededge/Red ^{S2} (NDVI rededge)	$(\text{Red edge} - \text{RED}) / (\text{Red edge} + \text{RED})$	[31]
Normalized Difference NIR/Rededge	$(\text{NIR} - \text{Red edge}) / (\text{NIR} + \text{Red edge})$	[32]
Normalized Difference Red-Edge ^{S2} (NDRE)		
Green Atmospherically Resistant Vegetation Index ^{L9} (GARI)	$(\text{NIR} - (\text{GREEN} - (\text{BLUE} - \text{RED}))) / (\text{NIR} - (\text{GREEN} + (\text{BLUE} - \text{RED})))$	[32]
Soil and Atmospherically Resistant Vegetation Index 2 ^{L9} (SARVI2)	$2.5 * (\text{NIR} - \text{RED}) / (1 + \text{NIR} + 6\text{RED} - 7.5 * \text{BLUE})$	[30]

Note: In the table, ^{S2} indicates that this vegetation index is the vegetation index used by Sentinel-2 alone, ^{L9} indicates the vegetation index is used by Landsat-9 alone. The others are used by both.

2.4.2. Model for Monitoring Pine Wilt Disease with Multi-Temporal Satellite Remote Sensing Data

In 2014, the pine wilt disease epidemic was first identified in Muping District, and since Sentinel-2 has no data before 2015, it was not chosen as the data source for multi-temporal analysis in this study. Twelve Landsat satellite data views from 2008 to 2013 (excluding 2011) and 2022 were utilized for multi-temporal analysis. Among them, 10 scenes of Landsat satellite data from 2008 to 2013 (excluding 2011) represented healthy years without pine wilt disease infestation, while two scenes of Landsat-9 satellite data from 2022 represented infested years. In accordance with a previous study (Yu et al., 2018) [33], four vegetation indices—RGI (Red–Green index), NDVI (Normalized Difference Vegetation Index), NDMI (Normalized Difference Moisture Index), and MSI (Moisture Stress Index)—were used for the classification of multi-temporal data (Table 4).

Table 4. Vegetation indices used in multi-temporal datasets.

Name	Formula	Ref.
Red–Green Index (RGI)	$\text{RED} / \text{GREEN}$	[34]
Normalized Difference Vegetation Index (NDVI)	$(\text{NIR} - \text{RED}) / (\text{NIR} + \text{RED})$	[35]
Normalized Difference Moisture Index (NDMI)	$(\text{NIR} - \text{MIR}) / (\text{NIR} + \text{MIR})$	[36]
Moisture Stress Index (MSI)	MIR / NIR	[37]

The methodology for computing differences in vegetation indices was as follows. Initially, we calculated the vegetation indices for samples in the 10 observed satellite views (2008–2013) separately, aiming to derive the 5-year averages of the vegetation indices during healthy years for these samples. We subtracted the vegetation index of a sample in the infestation year (2022) from the 5-year average vegetation index of that sample during

healthy years. This yielded the difference in the multi-temporal vegetation index for the sample, and this difference served as the dataset for multi-temporal analysis.

In this study, to boost the model's performance, we merged the multi-temporal dataset with the single-temporal dataset. In step (2), we chose the vegetation index difference dataset with the model's optimal performance and integrated it with Landsat-9's single-temporal dataset from 2022, forming a new dataset. This new dataset, combined with the three aforementioned machine learning algorithms, was employed to build a monitoring model for detecting pine wilt disease infestation in forest stands.

2.5. Validating Model Accuracy

In this study, three machine learning algorithms—artificial neural network (ANN), random forest (RF), and support vector machine (SVM)—were utilized to construct a monitoring model for pine wilt disease-infested forest stands. ANN achieves distributed and parallel information processing by mimicking the behavioral characteristics of animal neural networks [38]; RF is an ensemble learning method built on the creation of multiple independent decision trees [39]. SVM achieves classification goals by mapping feature data from low-dimensional spaces to high-dimensional spaces through a nonlinear mapping function [40]. We implemented the three algorithms using the “nnet”, “randomForest”, and “e1071” packages in R 4.3.2 software (RStudio, Inc., Boston, MA, USA). We defined the architecture and other hyperparameter values for ANN as follows: size = 2, rang = 0.1, decay = 5×10^{-4} , maxit = 200. The mtry and ntree parameters of RF were set to their default values, representing the square root of the number of features and 500 trees, respectively. For the SVM model, we selected a linear kernel function, and the cost parameter was set to 10^2 [41].

In this study, the dataset was split into a training set and a test set in a 7:3 ratio, and the model's performance was assessed using two indices: Accuracy and Kappa coefficient. The formulas for these indices are provided below.

Accuracy:

$$\text{Accuracy} = \frac{\text{TP} + \text{TN}}{\text{TP} + \text{TN} + \text{FP} + \text{FN}} \times 100\%$$

Here, TP denotes the number of true positives, TN represents the number of true negatives, FP is the count of false positives, and FN stands for the number of false negatives.

Kappa coefficient:

$$\text{Kappa} = \frac{P_0 - P_e}{1 - P_e}$$

Here, P_0 represents the overall classification accuracy, and P_e is calculated by adding the sum of the products of the predicted and actual numbers for each category, divided by the square of the total number of samples.

3. Results

3.1. Impact of Different Data Sources on Model Accuracy

Landsat-9 and Sentinel-2 data at 30 m spatial resolution were processed using three algorithms: ANN, RF, and SVM. The results indicated no significant difference in accuracy between Landsat-9 and Sentinel-2 data across the three algorithms (Figure 3). Detailed results can be found in Table S1 of the Supplementary Materials. Among them, the Sentinel-2 model constructed using the RF achieved the highest accuracy rate of 78.91%, while the Landsat-9 model with the highest accuracy rate was built using the ANN, reaching an accuracy rate of 77.87%. Additionally, to investigate the contribution of feature parameters to the accuracy of the Sentinel-2 model, we ranked the parameters in the Sentinel-2 dataset based on random forest importance (Figure 4). The top five parameters were CLI, NGRDI, RED, SWIR-1, and SLAV1, indicating that the red band, short-infrared band, and their corresponding vegetation indices had a notable impact on the sensitivity of detecting pine wilt disease-infested stands.

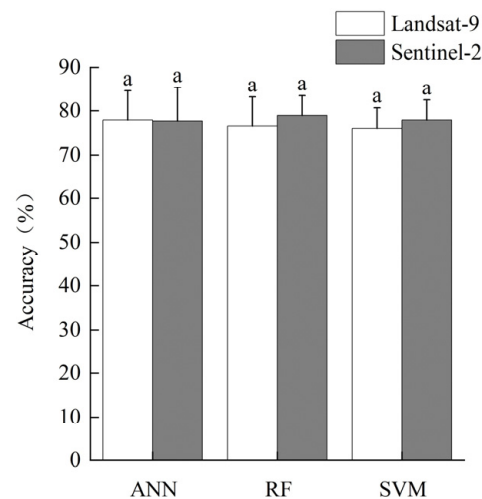


Figure 3. Accuracy and significance analysis of Landsat-9 and Sentinel-2 models based on different algorithms at a resolution of 30 m. a: Pairwise differences in model accuracy among various monitoring models.

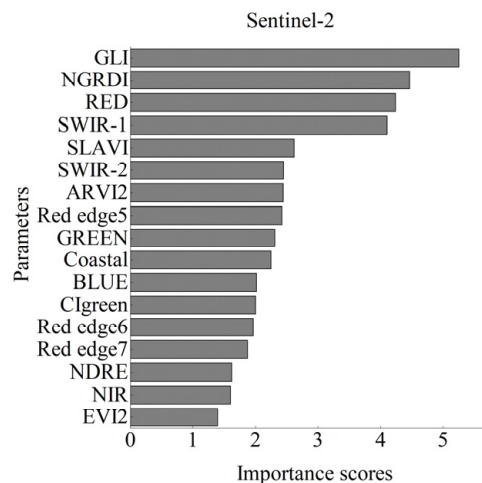


Figure 4. Sentinel-2 parameter importance ranking.

3.2. Effects of Satellite Remote Sensing Data Resolution on Model Accuracy

One advantage of Sentinel-2 data over Landsat data is the ability to achieve higher spatial resolution through resampling. This study compared the discrimination accuracy of models constructed from 10 m and 30 m resolution Sentinel-2 data. The results of a one-way ANOVA revealed that the discriminative accuracy of 10 m resolution Sentinel-2 data was significantly higher than that of 30 m resolution data for both the ANN and RF algorithms, showing an improvement in accuracy of 7.51% (ANN) and 6.49% (RF), respectively (Figure 5). Detailed results can be found in Table S2 of the Supplementary Materials. In general, as the spatial resolution of Sentinel-2 increased, there was an improvement in the accuracy of the corresponding model.

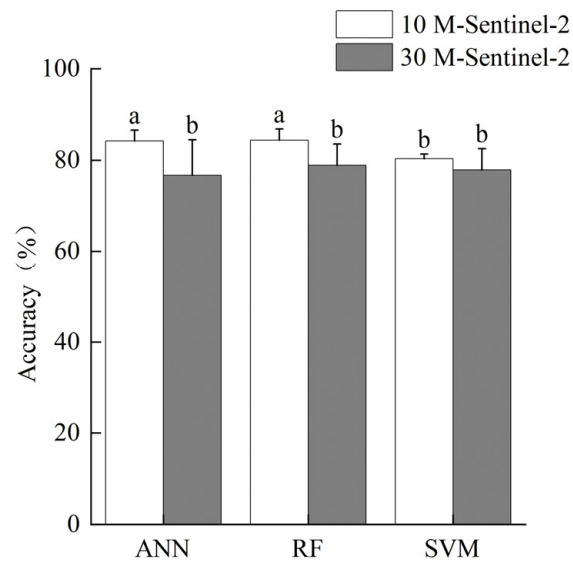


Figure 5. Accuracy of the Sentinel-2 model at different resolutions and significance analysis. a,b: Pairwise differences in model accuracy among various monitoring models.

3.3. Analysis of Single-Temporal, Multi-Temporal, and Combined Single-Temporal and Multi-Temporal Landsat Datasets

Figure 6 shows the disparities in vegetation indices between healthy and infested sample plots. Using the RGI difference as an example, the vegetation index difference in healthy plots predominantly falls within the range of -0.5 to 0 , while in infested sample plots, the difference is mainly in the range of 0 to 0.4 (greater than 0). This implies that following infestation with pine wilt disease, the RGI values in the forest stand increase. Similarly, after infestation with pine wilt disease, the MSI values increase, while the NDVI and NDMI values decrease.

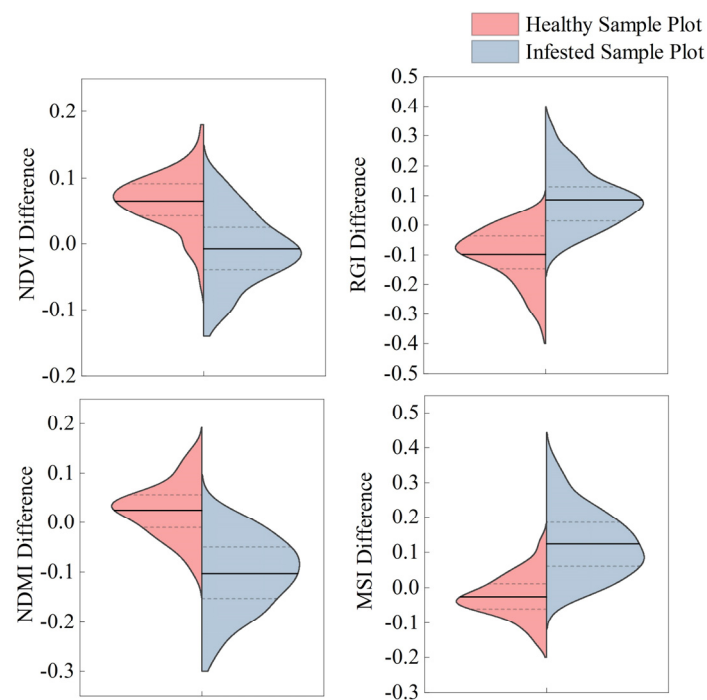


Figure 6. Distribution of differences in vegetation indices between healthy and infested sample plots.

As for differences between datasets under various machine learning algorithms, the accuracy of RGI difference exceeds that of NDVI difference under all algorithms. The optimal multi-temporal model was constructed using RGI difference combined with the support vector machine algorithm, achieving a model accuracy of 85.95%. This accuracy is higher than that of the optimal models of NDVI, NDMI, and MSI by 3.98%, 1.99%, and 0.62%, respectively.

The model accuracy of four vegetation index difference datasets under various machine learning algorithms is depicted in Figure 7 (Detailed results can be found in Table S3 of the Supplementary Materials). Among all algorithms, the accuracy of RGI difference is notably higher than that of NDVI difference. Moreover, with the exception of the RF, the accuracy of multi-temporal RGI difference models is significantly higher than that of single-temporal Landsat models (Figure 7); it exceeds the latter by 8.30% (Detailed results can be found in Table S4 of the Supplementary Materials). To identify the optimal model, this study integrated single-temporal data with multi-temporal data, creating a new dataset by combining RGI difference with the 2022 Landsat-9 single-temporal dataset to construct a new model. One-way ANOVA results indicated that the accuracy of the model constructed by combining single-temporal and multi-temporal phase data was significantly higher than that of the single-temporal phase alone. The optimal model emerged from combining RGI difference with the ANN, boasting a model accuracy of 88.26%. This represents a notable improvement of 10.61% over the optimal single-temporal phase model (utilizing the ANN) and 2.31% over the optimal multi-temporal phase model. In the importance ranking of feature parameters (Figure 8), RGI difference attained the highest importance score, signifying its significant contribution to the model constructed by integrating single-temporal and multi-temporal data (Figure 8). Detailed results can be found in Table S5 of the Supplementary Materials.

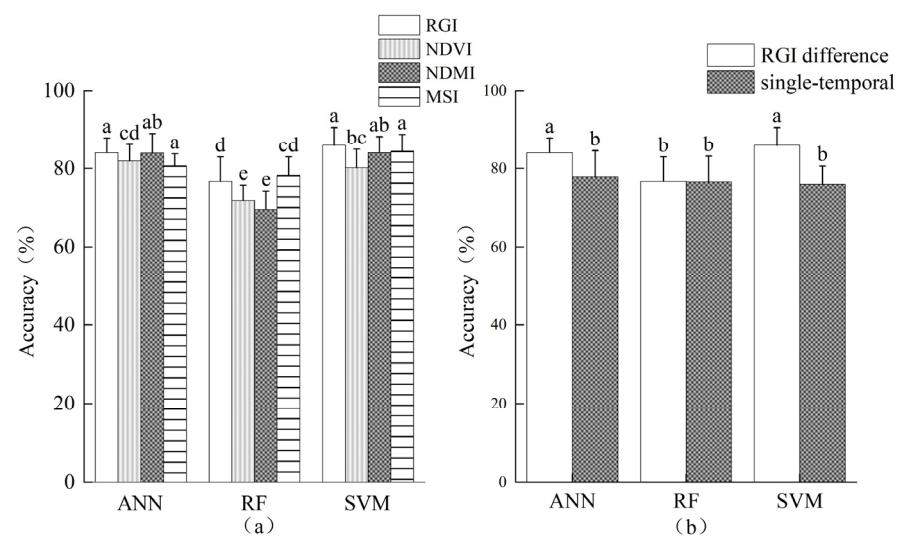


Figure 7. (a) Accuracy as well as significance analysis of models constructed under different machine learning algorithms for four multi-temporal Landsat datasets. (b) Accuracy and significance analysis of optimal multi-temporal model and optimal single-temporal model for Landsat datasets. a–e: Pairwise differences in model accuracy among various monitoring models.

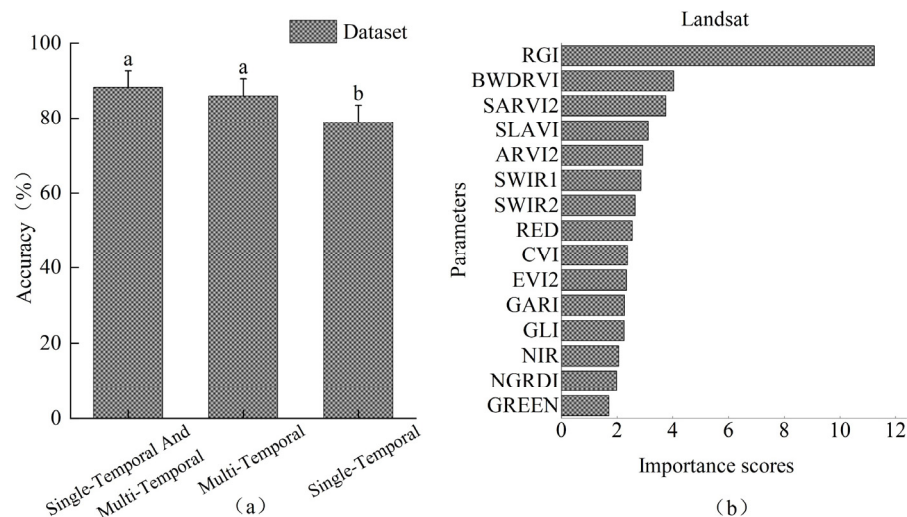


Figure 8. (a) Accuracy and significance analysis of optimal models constructed based on different datasets. (b) Importance ranking of feature parameters in single-temporal combined with multi-temporal dataset. a,b: Pairwise differences in model accuracy among various monitoring models.

4. Discussion

In this study, utilizing single-temporal Landsat-9 and Sentinel-2 images alongside multi-temporal Landsat images, we investigated variations among datasets for monitoring pine wilt disease-infested stands. This exploration covered diverse factors such as data sources, resolutions, and the distinction between single-temporal and multi-temporal data.

The experimental results revealed that medium-resolution Landsat images and Sentinel-2 images can effectively distinguish pine wilt disease-infested forest stands. Additionally, there was minimal difference in the accuracy of models constructed at 30 m resolution. In comparison to Landsat-9, Sentinel-2 was equipped with three additional red-edge bands. These bands, situated between the red and near-infrared bands, have been indicated in some studies to exhibit greater sensitivity to the growth of green vegetation [42]. Nevertheless, at a spatial resolution of 30 m, the accuracy of the model built from single-temporal Sentinel-2 data is comparable to that of single-temporal Landsat-9 data. The red-edge band ranks lower in importance, with its contribution to the Sentinel-2 monitoring model being less pronounced compared to the red band and the short-wave infrared band (Figure 4). Concurrently, in the artificial neural network and random forest algorithms, the accuracy of the model built from the Sentinel-2 dataset at 10 m resolution markedly exceeds that at 30 m resolution. This is attributed to the availability of more pine wilt disease-infested image pixels, richer spatial texture information, and finer detection of geometrical features in 10 m resolution images for feature identification and classification [43]. Hence, the accurate identification of pine stands infested by pine wilt disease is attainable. This approach reduces the manpower and material resources needed for surveying infected areas, thereby achieving more precise management.

Additionally, within the multi-temporal phase dataset, the RGI difference proves to be the most sensitive indicator for detecting pine wilt disease-infested stands. NDMI and MSI are associated with the short-wave infrared and near-infrared bands, reflecting vegetation moisture status [33,36]. In contrast, NDVI relates to the near-infrared and red bands, with values typically ranging from -1 to 1 , indicating vegetation health [44]. Nevertheless, the multi-temporal model constructed using the differences in NDMI, MSI, and NDVI performed less effectively compared to the model constructed using the difference in RGI. The satellite images utilized in this study predominantly originate from September and October each year, a period when infested trees are typically in the late stage of disease susceptibility. During this time, the color of tree crowns tends to be predominantly red. The Red–Green Index (RGI) is the ratio of the red and green bands. After infestation with pine

wilt disease, the chlorophyll absorption band intensity in pine trees is notably low, leading to increased reflectivity of the red band [6]. Consequently, a substantial difference in RGI between healthy and infested pixels is observed, with a pronounced distinction between the two.

In this experiment, model accuracy derived from the multi-temporal Landsat dataset markedly exceeded that of the single-temporal Landsat dataset. Moreover, the amalgamation of the single-temporal and multi-temporal Landsat datasets led to a further enhancement in the accuracy of monitoring pine wilt disease-infested stands. The findings of this study align with those of previous research on pest and disease monitoring. Previous studies have demonstrated that monitoring performance using a multi-temporal Landsat dataset is notably superior to a single-temporal Landsat dataset in stands (with 20%–80% tree mortality) moderately infested by the central European mountain pine beetle (*Dendroctonus ponderosae* Hopkins) [45]. Additionally, Hart et al. uncovered, based on abundant historical Landsat data, that drought triggered an outbreak of the red fat borer (*Dendroctonus rufipennis*) in a manner that single-temporal satellite data could not achieve [46]. In the monitoring of pine wilt disease, Qiu et al. used single-temporal Landsat-8 and Sentinel-2 satellite data along with employing multiple machine learning algorithms to develop monitoring models for pine wilt disease-infested stands. However, they did not fully exploit the rich historical data available from Landsat satellites [18]. Compared to previous studies, in this research study utilizing multi-temporal Landsat satellite data, we clarified the benefits of multi-temporal Landsat remote sensing data in monitoring forest stands infested with pine wilt disease. This clarification led to an improvement in the performance of medium-resolution satellite monitoring models.

The results of this experiment can contribute to a more precise management of pine wilt disease, offering a more accurate detection of PWD-infested forest stands. Meanwhile, the usage of open-source satellite images can reduce the cost, showing a strong economic applicability. Consequently, it helps slow down the spread of pine wilt disease. Moreover, the findings from this experiment can serve as a technical reference for future studies on multi-temporal monitoring of pine wilt disease and preventing its further dissemination. Xu et al. conducted pine wilt disease-infested disease stand monitoring using Landsat-8 TIRS remote sensing data (thermal infrared data). Their findings revealed that thermal infrared remote sensing detected pine wilt disease-infested stands earlier than multispectral Landsat satellite data [47]. A narrower sensor bandwidth is more advantageous for distinguishing and identifying ground objects. In comparison to multispectral satellites, hyperspectral satellites offer higher spectral resolution and observation channels, providing additional information for pest and disease monitoring [48]. In our upcoming research phase, we will explore the capabilities of multiple sensors in monitoring pine wilt disease-infested forest stands. Testing the constructed model in various regions will enable us to refine the model further, offering technical support for monitoring pine wilt disease-infested forest stands.

Supplementary Materials: The following supporting information can be downloaded at: <https://www.mdpi.com/article/10.3390/f15040596/s1>, Table S1. ANOVA results of different models for Landsat-9 and Sentinel-2. Table S2. ANOVA of model accuracy for Sentinel-2 at different resolutions. Table S3. ANOVA of multi-temporal model accuracy. Table S4. ANOVA of the accuracy of Landsat single-temporal and multi-temporal models. Table S5. ANOVA of the accuracy of three models.

Author Contributions: Conceptualization, L.Y.; data curation, J.K.; investigation, J.K. and D.W.; methodology, J.K. and L.Y.; resources, Q.Z. and Y.L.; formal analysis, J.K.; supervision, Y.L.; validation, L.Y.; writing—original draft, J.K.; writing—review and editing, L.Y. and L.R.; project administration, Y.L. All authors have read and agreed to the published version of the manuscript.

Funding: This research was funded by National Key R&D Program of China (2022YFD1400400).

Data Availability Statement: The data presented in this study are available on request from the corresponding author. The data are not publicly available currently due to funding requirements.

Acknowledgments: The authors would like to thank Linfeng Yu, Quan Zhou, and Dewei Wu for their help and advice in the study.

Conflicts of Interest: The authors declare no conflicts of interest.

References

- Liu, X.L.; Cheng, D.X.; Li, T.; Chen, X.P.; Gao, W.J. Preliminary study on automatic monitoring trees infected by pine wood nematode with high resolution images from unmanned aerial vehicle. *For. Pest Dis.* **2018**, *37*, 16–21.
- Zhang, L.H.; Lin, R.F.; Huang, D.D.; Zhang, Y.Z.; Lai, J.H.; Liu, L.L.; Zhang, S.S. Progress in the Identification of Pathogenic Nematodes of Pine Wood Nematode Diseases. *Biol. Disaster Sci.* **2023**, *46*, 236–241.
- Ye, J.R.; Wu, X.Q. Research progress of pine wilt disease. *For. Pest Dis.* **2022**, *41*, 1–10. [\[CrossRef\]](#)
- National Forestry and Grassland Administration Announcement (No. 6 of 2022) (Pine Wormwood Nematode Infected Areas 2022). Available online: <https://www.forestry.gov.cn/c/www/gkzfwj/272539.jhtml> (accessed on 1 September 2023).
- Li, S.; Sun, H.; Zhou, Y.; Li, X.; Yu, Z.; Dong, Z. Occurrence of major forestry pests in China in 2021 and forecast of their occurrence trend in 2022. *For. Pest Dis.* **2022**, *41*, 44–47.
- Zhang, J.C.; Yuan, L.; Wang, J.H.; Luo, J.H.; Du, S.Z.; Huang, W.J. Research progress of crop diseases and pests monitoring based on rem sensing. *Trans. Chin. Soc. Agric. Eng.* **2012**, *28*, 1–11.
- Shu, M.; Zhang, D.Q.; Xu, Q.R.; Tang, X.H. Research Progress in the Diagnosis and Monitoring of *Bursaphelenchus xylophilus* Based on Remote Sensing Technology. *Anhui Agric. Sci.* **2022**, *50*, 11–14.
- Xu, H.C.; Luo, Y.Q.; Zhang, T.T.; Shi, Y.J. Changes of Reflectance Spectra of Pine Needles in Different Stage after Being Infected by Pine Wood Nematode. *Spectrosc. Spectr. Anal.* **2011**, *31*, 1352–1356.
- Yu, R.; Ren, L.; Luo, Y.Q. Early detection of pine wilt disease in *Pinus tabulaeformis* in North China using a field portable spectrometer and UAV-based hyperspectral imagery. *For. Ecosyst.* **2021**, *8*, 44. [\[CrossRef\]](#)
- Wang, J.; Chen, R.F.; Chen, Q.; Li, Y.H.; Zhang, C. Research on Forest Parameter Information Extraction Progress Driven by UAV Remote Sensing Technology. *For. Resour. Manag.* **2020**, *5*, 144–151. [\[CrossRef\]](#)
- Wu, W.; Zhang, Z.; Zheng, L.; Han, C.; Wang, X.; Xu, J.; Wang, X. Research Progress on the Early Monitoring of Pine Wilt Disease Using Hyperspectral Techniques. *Sensors* **2020**, *20*, 3729. [\[CrossRef\]](#)
- Li, T. Monitoring technology of pine wood nematode disease based on UAV hyperspectratechnology. *Geomat. Technol. Equip.* **2023**, *25*, 19–21. [\[CrossRef\]](#)
- Iordache, M.-D.; Mantas, V.; Baltazar, E.; Pauly, K.; Lewycky, N. A Machine Learning Approach to Detecting Pine Wilt Disease Using Airborne Spectral Imagery. *Remote Sens.* **2020**, *12*, 2280. [\[CrossRef\]](#)
- Fang, G.F.; Huang, W.J.; Mu, X.W.; Liu, H.A.; Zhou, H.B.; Zhang, J.Q.; Zhang, B.Y.; Li, X.D.; Chen, Y.F. Practice and prospect of precise monitoring of pine wilt disease. *For. Pest Dis.* **2022**, *41*, 16–23. [\[CrossRef\]](#)
- Zhang, B.Y.; Ye, H.C.; Lu, W.; Huang, W.J.; Wu, B.; Hao, Z.Q.; Sun, H. A Spatiotemporal Change Detection Method for Monitoring Pine Wilt Disease in a Complex Landscape Using High-Resolution Remote Sensing Imagery. *Remote Sens.* **2021**, *13*, 2083. [\[CrossRef\]](#)
- Qu, C.M.; Zhu, R.F.; Xu, Z.S.; Gui, Z.Q.; Song, W.L. Application of JiLin-1 satellite in monitoring discolored standing trees in pine forests in central and eastern Jilin Province. *Satell. Appl.* **2022**, *30*, 35–41.
- Jiao, Q.J.; Zheng, Y.F.; Huang, W.J.; Zhang, B.; Zhang, H.Y.; Shi, Y.M.; Wu, F.Y.; Fu, A.M. Detection of Discolored Trees Caused by Pine Wilt Disease Based on Vegetation Index Method Using Terrestrial Ecosystem Carbon Inventory Satellite Data. *For. Resour. Manag.* **2023**, *4*, 123–131. [\[CrossRef\]](#)
- Qiu, W.L.; Zhong, S.X. Based on multispectral satellite images and machine learning algorithms to recognize pine wood nematode disease affected stands. *J. Environ. Entomol.* **2023**, *45*, 408–420.
- Chen, W.J. Region Identification of *Dendrolimus superans* Pest Based on Multispectral Remote Sensing Images. Bachelor’s Thesis, Northeast Forestry University, Harbin City, China, 2021.
- Lin, X.B.; Sun, J.H.; Yang, L.; Liu, H.; Wang, T.; Zhao, H. Application of UAV Multispectral Remote Sensing to Monitor Damage Level of Leaf-feeding Insect Pests of Oak. *J. Northeast For. Univ.* **2023**, *51*, 138–144. [\[CrossRef\]](#)
- Abdullah, H.; Skidmore, A.K.; Darvishzadeh, R.; Heurich, M. Sentinel-2 accurately maps green-attack stage of European spruce bark beetle (*Ips typographus* L.) compared with Landsat-8. *Remote Sens. Ecol. Conserv.* **2019**, *5*, 87–106. [\[CrossRef\]](#)
- Yantai Muping District People’s Government Office on the Issuance of “Yantai Muping District 2020 Annual Pine Woodworm Disease Prevention and Control Implementation Program” Notice. Available online: http://www.muping.gov.cn/art/2020/8/5/art_100808_23022.html (accessed on 10 September 2023).
- Tian, Q.J.; Min, X.J. Advances in study on vegetation indices. *Adv. Earth Sci.* **1998**, *14*, 327–333.
- Datt, B.; McVicar, T.R.; Van Niel, T.G.; Jupp, D.L.; Pearlman, J.S. Preprocessing EO-1 Hyperion hyperspectral data to support the application of agricultural indexes. *IEEE Trans. Geosci. Remote Sens.* **2003**, *41*, 1246–1259. [\[CrossRef\]](#)
- Baroni, F.; Boscagli, A.; Di Lella, L.A.; Protano, G.; Riccobono, F. Arsenic in soil and vegetation of contaminated areas in southern Tuscany (Italy). *J. Geochem. Explor.* **2004**, *81*, 1–14. [\[CrossRef\]](#)
- Hancock, D.W.; Dougherty, C.T. Relationships between blue- and red-based vegetation indices and leaf area and yield of alfalfa. *Crop Sci.* **2007**, *47*, 2547–2556. [\[CrossRef\]](#)

27. Ahamed, T.; Tian, L.; Zhang, Y.; Ting, K. A review of remote sensing methods for biomass feedstock production. *Biomass Bioenergy* **2011**, *35*, 2455–2469. [[CrossRef](#)]
28. Kaufman, Y.J.; Tanre, D. Atmospherically resistant vegetation index (ARVI) for EOS-MODIS. *IEEE Trans. Geosci. Remote Sens.* **1992**, *30*, 261–270. [[CrossRef](#)]
29. Miura, T.; Yoshioka, H.; Fujiwara, K.; Yamamoto, H. Inter-comparison of ASTER and MODIS surface reflectance and vegetation index products for synergistic applications to natural resource monitoring. *Sensors* **2008**, *8*, 2480–2499. [[CrossRef](#)] [[PubMed](#)]
30. Lymburner, L.; Beggs, P.J.; Jacobson, C.R. Estimation of canopy-average surface-specific leaf area using Landsat TM data. *Photogramm. Eng. Remote Sens.* **2000**, *66*, 183–192.
31. Chevrel, S.; Belocky, R.; Grösel, K. Monitoring and assessing the environmental impact of mining in Europe using advanced earth observation Techniques-MINEO, first results of the alpine test site. *Environ. Commun. Inf. Soc. EnviroInfo Vinee* **2002**, 518–526.
32. Hunt, E.R., Jr.; Daughtry, C.S.T.; Eitel, J.U.H.; Long, D.S. Remote Sensing Leaf Chlorophyll Content Using a Visible Band Index. *Agron. J.* **2011**, *103*, 1090–1099. [[CrossRef](#)]
33. Yu, L.; Huang, J.X.; Zong, S.X.; Huang, H.G.; Luo, Y.Q. Detecting Shoot Beetle Damage on Yunnan Pine Using Landsat Time-Series Data. *Forests* **2018**, *9*, 39. [[CrossRef](#)]
34. Coops, N.C.; Johnson, M.; Wulder, M.A.; White, J.C. Assessment of QuickBird high spatial resolution imagery to detect red attack damage due to mountain pine beetle infestation. *Remote Sens. Environ.* **2006**, *103*, 67–80. [[CrossRef](#)]
35. Tucker, C.J. Red and photographic infrared linear combinations for monitoring vegetation. *Remote Sens. Environ.* **1979**, *8*, 127–150. [[CrossRef](#)]
36. Wilson, E.H.; Sader, S.A. Detection of forest harvest type using multiple dates of Landsat TM imagery. *Remote Sens. Environ.* **2002**, *80*, 385–396. [[CrossRef](#)]
37. Rock, B.N.; Vogelmann, J.E.; Williams, D. Field and Airborne Spectral Characterization of Suspected Damage in Red Spruce (*Picea rubens*) from Vermont. 1985. Available online: <https://ntrs.nasa.gov/citations/19860052270> (accessed on 1 September 2022).
38. Chen, K. Image Recognition and Generation Based on Artificial Intelligence Algorithms. *Comput. Knowl. Technol.* **2018**, *14*, 173–175. [[CrossRef](#)]
39. Gu, T.H.; Du, X.L.; Li, L.; Zhu, Y.L.; Zhang, Y.M.; Wu, C.H. Classification of Satellite Cloud Image Based on Texture Features and Machine Learning. *Mid-Low Latit. Mt. Meteorol.* **2023**, *47*, 50–55.
40. Mu, D.X.; Yang, L.; Wu, Z.Q. Apple surface defect detection based on improved multi-scale Retinex image enhancement and support vector machine. *J. Food Saf. Qual.* **2023**, *14*, 183–191. [[CrossRef](#)]
41. Zhan, Z.; Yu, L.; Li, Z.; Ren, L.; Gao, B.; Wang, L.; Luo, Y. Combining GF-2 and Sentinel-2 Images to Detect Tree Mortality Caused by Red Turpentine Beetle during the Early Outbreak Stage in North China. *Forests* **2020**, *11*, 172. [[CrossRef](#)]
42. Duan, J.K.; Li, F.; Qin, Q.; Hu, X.F.; Wang, H.; Han, D.F.; Gu, C. Effect of GF-6 red-edge bands on identification of summer maize planting area. *J. Mar. Meteorol.* **2023**, *43*, 104–112. [[CrossRef](#)]
43. Chen, L.; Jia, J.; Wang, H.Q. An overview of applying high resolution remote sensing to natural resources survey. *Remote Sens. Land Resour.* **2019**, *31*, 37–43.
44. Sun, F.Y.; Wang, Z.H.; Fu, W.; Li, X.S. Development and Application of Settlement Index of Forest Pests and Diseases for Large Areas through Using MODIS-NDVI Data. *For. Resour. Manag.* **2017**, *6*, 149–152+158. [[CrossRef](#)]
45. Meddens, A.J.H.; Hicke, J.A.; Vierling, L.A.; Hudak, A.T. Evaluating methods to detect bark beetle-caused tree mortality using single-date and multi-date Landsat imagery. *Remote Sens. Environ.* **2013**, *132*, 49–58. [[CrossRef](#)]
46. Hart, S.J.; Veblen, T.T.; Schneider, D.; Molotch, N.P. Summer and winter drought drive the initiation and spread of spruce beetle outbreak. *Ecology* **2017**, *98*, 2698–2707. [[CrossRef](#)]
47. Zhao, X.; Huang, H.G.; Wang, J.X.; Su, A.N. Early Response of Thermal Infrared Remote Sensing to Pine Wood Nematode in *Pinus massoniana* Forest. *J. Northwest For. Univ.* **2023**, *38*, 166–172.
48. Hank, T.B.; Berger, K.; Bach, H.; Clevers, J.G.P.W.; Gitelson, A.; Zarco-Tejada, P.; Mauser, W. Spaceborne Imaging Spectroscopy for Sustainable Agriculture: Contributions and Challenges. *Surv. Geophys.* **2019**, *40*, 515–551. [[CrossRef](#)]

Disclaimer/Publisher’s Note: The statements, opinions and data contained in all publications are solely those of the individual author(s) and contributor(s) and not of MDPI and/or the editor(s). MDPI and/or the editor(s) disclaim responsibility for any injury to people or property resulting from any ideas, methods, instructions or products referred to in the content.